*Chapter 5*

# OPTICAL CHARACTERISTICS OF TRACKS IN SOLID STATE NUCLEAR TRACK DETECTORS STUDIED WITH RAY TRACING METHOD

## *D. Nikezic and K.N. Yu*

Department of Physics and Materials Science, City University of Hong Kong
Tat Chee Avenue, Kowloon, Hong Kong.

## ABSTRACT

Although the optical microscope has been the main tool for observations of etched tracks in solid state nuclear track detectors for many years, there has been relatively little investigation about the optical characteristics of these tracks. This chapter describes the application of the ray tracing method to light propagation through these etched tracks. The method is shown to be able to reproduce track appearances and to give distributions of scattered light from a single track as well as from an assembly of tracks. The ray tracing method as well as the methodology in creating a 3-D mesh to represent a track are given with more details. Some representative examples in determining the track appearance and the scattered light distribution are shown.

## 1. INTRODUCTION

For radon measurements and many other applications, etched tracks in solid state nuclear track detectors (SSNTDs) were studied using optical microscopes (see e.g., Yu et al., 2005). However, as expected, the procedures involved were tedious and time consuming. Automatic and semi-automatic systems are desirable, but the optical appearance of tracks or the scattered light intensity are involved.

Although the use of the microscope is almost compulsory, there have been only few studies on light propagation through the etched tracks. McNulty et al. (1982) anticipated the importance of total reflection in the formation of the track images. Fews (1992) used the "mean optical density" measured by an image analysis system as an additional parameter in

track studies to extend the data available for α particles and protons. An "average brightness" of a single track was introduced to distinguish among various types of charged particle tracks by Skvarč et al. (1992). The optical properties of a single track obtained by neutron radiography were also discussed by Assunção et al. (1994). Skvarč (1999) developed a model to determine the visual appearance of the track by using the freeware software POVRAY.

There exist only a few references in the literature on scattering of light from etched tracks in SSNTDs. In most of the cases, scattered light was used to measure the track densities from experiments related to neutron dosimetry (Harvey and Weeks, 1987; Popov and Pressyanov, 1997; Meyer et al., 1997; Groetz et al., 1999). Groetz et al. (1998) developed a model for laser light scattering by nuclear tracks in CR-39 detectors. The model was based on wave optics and the so-called "*bi-directional scatter distribution function*" to describe scattered light patterns in two orthogonal planes.

Recently a model based on geometrical optics to simulate light propagation through the etched tracks, and to calculate brightness levels of track elements and the whole track was developed (Nikezic et al., 2005, Yu et al., 2007). The model was further extended and computer programs were developed to determine the distribution of scattered light from one single track and also from an assembly of tracks. These models will be discussed in the sections below, and some illustrative data will be presented.


## 2. SOLID STATE NUCLEAR TRACK DETECTORS

### 2.1. Basics

Swift heavy charged particles can ionize the materials through which they pass. The ionization may be very extensive depending on the energy, charge and mass of the ionizing particle and the properties of the traversed medium. Several ion pairs may be created per 1 nm, indicating that almost all molecules traversed by the particle are ionized. Ionizations may be followed by dissociation of molecules and a series of new chemical processes that create free chemical radicals and other chemical species. Cross-linking between molecules is also possible. Along the path of a charged particle, a damaged zone enriched with free chemical radicals and other chemical species is then created. This damaged zone is a latent track. By using an electronic microscope, a latent track may be seen as a narrow scratch, with a dimension of several *nm*, in the body of the detector.

If a material with latent tracks is exposed to some chemically aggressive solution, chemical reactions would be more intense along these latent tracks, although the undamaged detector surface is also etched away at the same time. Due to enhanced chemical activity, etching along the latent track progresses with a larger rate than the undamaged detector surface. In this way, a "track" of the particle is formed upon etching, which may be seen as an etch pit or as a hole under an optical microscope with magnification of a few hundred times. Exposing the detector to a chemically aggressive solution is referred to as "detector etching". As a final result, the tracks become visible. They may be counted or studied in more details under the optical microscope. Creation of a latent track which can be enlarged by chemical or electrochemical etching is referred to as the "track effect". The occurrence of latent tracks was discovered in a LiF crystal by Young (1958). One year later, Silk and Barnes (1959)

reported the identification of damaged regions in mica caused by heavy charged particles through the use of the transmission electron microscope. Fleischer et al. (1965) extensively studied this method, and applied the method to mica as well as other materials such as minerals, plastics and glasses.

The track effect exists in many materials and is best manifested in materials with long molecules, the latter thus being the best solid state nuclear track detectors. Some amorphous materials like glasses, and some natural minerals like mica, apatite or olivine, also demonstrate the track effect. Dielectric materials are the commonest materials showing the track effect.

The track effect has been extensively investigated. Many materials were examined and some are used for commercial manufacturing of detectors. One of the most frequently used detectors is the polyallyldiglycol carbonate (PADC) (commercially available as the CR-39 detector) discovered by Cartwright et al. (1978). Another frequently used detector is cellulose nitrate which is the basic material employed for the commercially available LR 115 detector. Other kinds of detectors commonly in use include polycarbonate, on which the commercially available Makrofol detector is based.

There have been various descriptions of these detectors, including solid state nuclear track detectors (SSNTDs), nuclear track detectors (NTDs), track etch detector (TEDs), etc. The description solid state nuclear track detectors (SSNTDs) will be used hereafter in this chapter. A review on SSNTDs was given by Nikezic and Yu (2004). Many applications with SSNTDs have been developed, including radon/radon progeny measurements, space investigation with particle identification, geology, seismology, uranium prospecting, nanotechnology, etc. (see e.g., Fleischer 1998).

## 2.2. Track Geometry

Since this chapter will discuss the simulation of light transport through the tracks based on geometrical optics, the geometry of a track itself is of primary importance. Track development from the geometrical point of view is similar to the creation of the wave pattern when a boat with a slowly varying velocity travels in water. The only difference is that the track is a three-dimensional structure while the wave formed is a two-dimensional phenomenon on the water surface. It has been established that the track development can be described with two etching rates, $V_b$ and $V_t$ (Fleischer et al., 1975). Here, $V_b$ is called the bulk etch rate, i.e., the etch rate of the undamaged detector surface; $V_t$ is called the track etch rate, i.e., the etch rate of along the latent track; both etch rates are usually given in the unit μm/h. The particle incidence onto the detector surface can be broadly categorized into normal incidence and oblique incidence. As regards the track etch, two cases can be considered, viz., constant $V_t$ and variable $V_t$. The most general case is variable $V_t$ and oblique incidence.

In order to introduce the basic terms, we will first briefly consider the normal incidence with a constant $V_t$, as shown in Figure 1. Here, I and I' are the surfaces of the detector before and after etching, $h$ is the thickness of the undamaged detector removed by etching, $L'$ is the distance traveled by the etching solution along the latent track, $L$ is the track depth, $O$ is the point where the particle enters the detector and $E$ is the point where the particle has brought to a stop in the detector, i.e., $OE$ is the particle range in the detector. During etching, the etchant progresses with the rate $V_t$ along the latent track while in all other directions it progresses

with the rate $V_b$. As a consequence of simultaneous actions of the etching solution, a conical track is formed with the angle of cone given by $\delta = \sin^{-1}(V_b/V_t)$. Considering the track geometry shown in Figure 1, the expression for the diameter $D$ of the track opening can be derived as:

$$D = 2h\sqrt{\frac{V-1}{V+1}}$$

(1)

where $V = V_t/V_b$.

The angle $\delta$ as defined above is also known as the critical angle for etching. When the particle incidence is oblique, and if the incident angle is smaller than $\delta$, no tracks can be developed. If the etching time is sufficiently long, the etching solution would be able to reach the end point $E$. Further etching will be in all directions with the bulk etch rate $V_b$, which will create a sphere with the center at point $E$. This sphere joins with the conical part of the track. With further etching, the size of the sphere will keep increasing and finally the entire track will become a part of a sphere. For normal incidence of the particle, the track opening is always circular regardless of the phase of track development.

For an oblique incidence, the etched track can be described with the same parameters as those above, but with some additional ones. Since the intersection between the cone and the plane $I'$ is an ellipse, the track opening will be an ellipse. Therefore, the track opening is characterized by two parameters, namely, the minor axis $d$ and the major axis $D$ of the ellipse. In the course of chemical etching, the track opening passes through several phases, with an elliptical appearance at the beginning. Upon further etching, when the sphere formed around the point $E$ touches the post-etching surface, the opening is partially an ellipse and partially a circle. With further etching, the circular part becomes larger, and the opening finally becomes fully circular when the track profile becomes completely a part of a sphere.
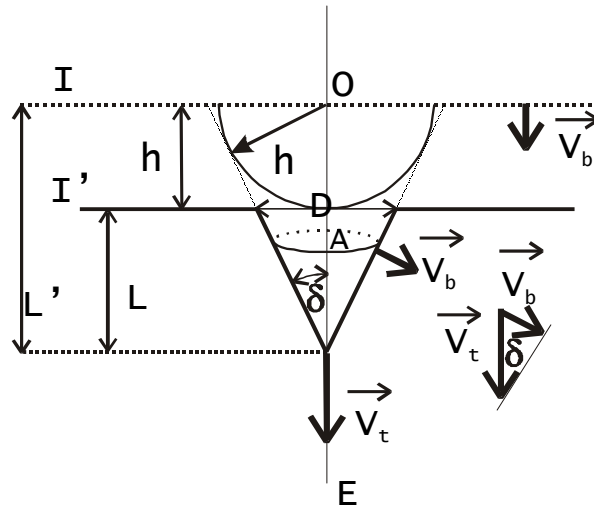


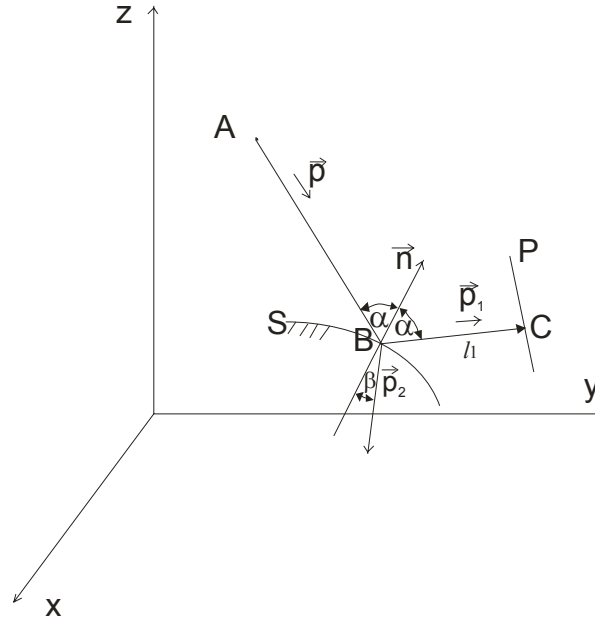Figure 1. Track etching for normal incidence and constant $V_t$.

Figure 2. Refraction and reflection of the ray on the spherical surface *S*.

When $V_t$ is variable, a more complex geometry is obtained. However, in most of the cases, $V_t$ varies "slowly", so the geometry for these cases are not very different from the special case where $V_t$ = constant.

Several models and mathematical treatments of track growth have been developed (Henke and Benton 1971, Somogy and Szalay 1973, Somogy 1980, Fews and Henshaw 1982, Fromm et al., 1988, Ditlov 1995, Nikezic and Yu 2003a). These models have been compared and have been found to produce similar results (Nikezic et al., 2006).


## 3. RAY TRACING METHOD

The ray tracing method generates an optical image by following different light rays through a particular medium, based on the laws of geometrical optics. Each light ray will have a "history" created through successive events of refraction and reflection it suffers at different surfaces. The method is extensively used in the design of optical devices.

To illustrate the application of this method, we consider the following example (see Figure 2) without going into all the details. The light ray comes from point *A* with coordinates $(x_A, y_A, z_A)$ and strikes the spherical surface *S* at some point *B*. The radius of the sphere is *R* with the center at the point $(x_S, y_S, z_S)$. The direction of the ray is described by the vector $\vec{p}$ with two polar angles $(\theta, \varphi)$. The task to be handled is to calculate the coordinates of point *C* on the planar screen *P* where this ray will intersect with *P* on the surface *C*, after refraction at point *B*. The equation of the line along which the ray travels between points *A* and *B* is given as

$$\frac{x - x_A}{p_x} = \frac{y - y_A}{p_y} = \frac{z - z_A}{p_z} = t \tag{2}$$

It is also known that $p_x = \sin\theta\cos\varphi;\ p_y = \sin\theta\sin\varphi$ and $p_z = \cos\theta$. The equation of the sphere $S$ is

$$(x - x_S)^2 + (y - y_S)^2 + (z - z_S)^2 = R^2 \tag{3}$$

The first step is to calculate the coordinates of point $B$ on the sphere.

By rearranging Eq. (2), i.e.,

$$x = x_A + t\,p_x;\ y = y_A + t\,p_y;\ z = z_A + tp_z \tag{4}$$

and substituting these into Eq. (3), a quadratic equation of $t$ can be found as

$$t^2 + 2t[p_x(x_A - x_S) + p_y(y_A - y_S) + p_z(z_A - z_S)] + \\ (x_A - x_S)^2 + (y_A - y_S)^2 + (z_A - z_S)^2 - R^2 = 0 \tag{5}$$

By solving Eq. (5), two solutions for $t$, namely $t_1$ and $t_2$, will be found. Replacing $t_1$ and $t_2$ in Eq. (4), the coordinates of two points, $B_1$ and $B_2$, where the line intersects with the spherical surface are determined. The point which is closer to $A$ will be the required point $B$, with the coordinates $(x_B, y_B, z_B)$.

The second step is to determine the normal vector, $\vec{n}$, on the sphere at point $B$. The incident angle between the incoming ray and the normal is determined through:

$$\cos\alpha = \vec{p} \cdot \vec{n} \tag{6}$$

with the assumption that the vectors $\vec{p}$ and $\vec{n}$ have a unit length.

The direction of the reflected ray, determined by the vector $\vec{p}_1$, has to be calculated from the following set of equations:

$$\vec{p}_1 \cdot (-\vec{p}) = \cos 2\alpha$$

$$\vec{p}_1 \cdot \vec{n} = \cos\alpha \tag{7}$$

$$\vec{p}_1 \cdot (\vec{p} \times \vec{n}) = 0.$$

The last equation means that all the three vectors $\vec{p}$, $\vec{n}$ and $\vec{p}_1$ are co-planar. The entire set of equations represents the law of reflection of light. From this set of equations, one can

find the $p_{1x}$, $p_{1y}$ and $p_{1z}$ components for the vector $\vec{p}_1$, which determine the direction of the reflected ray. The equation of the line $l_1$ along which the reflected ray propagates is

$$\frac{x - x_B}{p_{1x}} = \frac{y - y_B}{p_{1y}} = \frac{z - z_B}{p_{1z}} = t_1 \qquad (8)$$

The last step is to determine the intersection between the line $l_1$ and the plane representing the screen $P$. The equation for the plane $P$ is $Ex + Fy + Gz + H = 0$, where the coefficients $E$, $F$ and $G$ are related to the normal on the plane $P$, and the coefficient $H$ is related to a point which belongs to $P$. As a result, the coordinates of the point $C$ could be found.

If the ray is refracted at point $B$, the direction of the refracted ray is determined by the vector $\vec{p}_2$ from the following set of equations:

$$\vec{p}_2 \cdot \vec{p} = \cos(\alpha - \beta)$$

$$\vec{p}_2 \cdot (-\vec{n}) = \cos\beta \qquad (9)$$

$$\vec{p}_2 \cdot (\vec{p} \times \vec{n}) = 0.$$

The last equation in this set means that all the three vectors must be co-planar. This set of equations represents the law of refraction of light.

This simplified model may be used for different refractive and/or reflective surfaces, with the only difference lying in the determination of the normal to the surface at a particular point. If the surface is not given by an analytical expression, the surface area has to be divided into small elements which can be considered a plane. It is not required that the elements are regular geometrical figures, such as squares. One such element is shown in Figure 3, and is determined by four known points $T_i$ with the corresponding coordinates $(x_i, y_i, z_i)$, where $i = 1, \ldots, 4$.
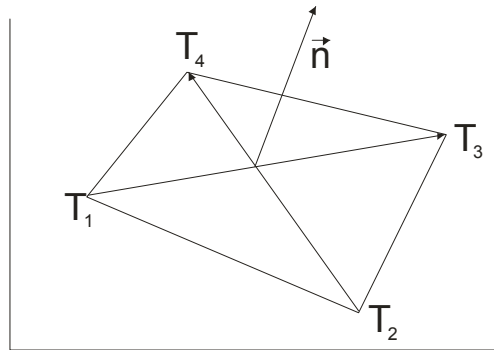


Figure 3. Determination of the normal to the polygonal element.

The vectors $\vec{T_1T_3}$ and $\vec{T_2T_4}$ are easily created with components $(x_3 - x_1, y_3 - y_1, z_3 - z_1)$

and $(x_4 - x_2, y_4 - y_2, z_4 - z_2)$. The vector product $\vec{T_1T_3} \times \vec{T_2T_4} = \vec{n}$ of these vectors is the normal $\vec{n}$ to the given surface element. All these vectors are normalized to have unit lengths. It is possible to use triangular elements instead of polygonal ones, but the methodology to determine the normal will be similar.

## 4. APPLICATION OF RAY TRACING METHOD TO PASSAGE OF LIGHT THROUGH TRACKS

The method described above is applied to the problem of light passage through the etched tracks. As it was mentioned in section 1, the dimensions of the latent tracks are several nm, up to 20 nm. After etching, the tracks are significantly enlarged to 10-30 μm, depending on the etching duration and other etching conditions. Since the yellow visible light has a wavelength of about $\lambda = (0.5 - 0.6)$ μm, one might conclude that the etched tracks have much larger dimensions than $\lambda$, and geometrical optics is valid for these objects. This, however, does not mean that effects of physical optics are never observed in track studies.

### 4.1. Formation of Three Dimensional Track Mesh

To apply the ray tracing method to the etched track, it is necessary to create a three-dimensional (3D) mesh which represents the track. To perform this task, a computer program should be written based on track growth models described above. In fact, it suffices to create points on the track wall on the plane which contains the trajectory of the particle and the major axis of the track opening. These points represent the track profile. In Figure 4, the line representing the track profile is denoted with $\mu$. The 3D track can then be obtained by rotating $\mu$ around the axis of the track, which is also the particle trajectory. During this rotation, circles are produced (from the points on $\mu$) and the coordinates of a selected number of points on these circles are stored in the computer memory. The circles are denoted with $AA'$ and $B'B''B$ in Figure 4(a). The entire set of these points forms a mesh to represent the track.

The 3D body of the track thus created intersects with the planes $\pi$, $\pi'$, $\pi''$ etc., which are parallel to the detector surface. The intersections between these horizontal planes and the 3D track are "horizontal" semi-elliptical curves, denoted by $\eta$, $\eta'$, $\eta''$, ... , which belong to the planes $\pi$, $\pi'$, $\pi''$, ..., respectively. The number of points representing each horizontal curve $\eta$ is kept constant. A mesh of triangles is then created from these points to represent the track wall, which is also schematically shown in Figure 4. The procedures of forming triangles are followed for the entire track. Some peculiarities will arise when triangles are formed between the last circle $\eta''$ and the tip of the track $T$. In this case, all triangles have one common point $T$ while the other two points of the triangles are neighboring points on $\eta''$.
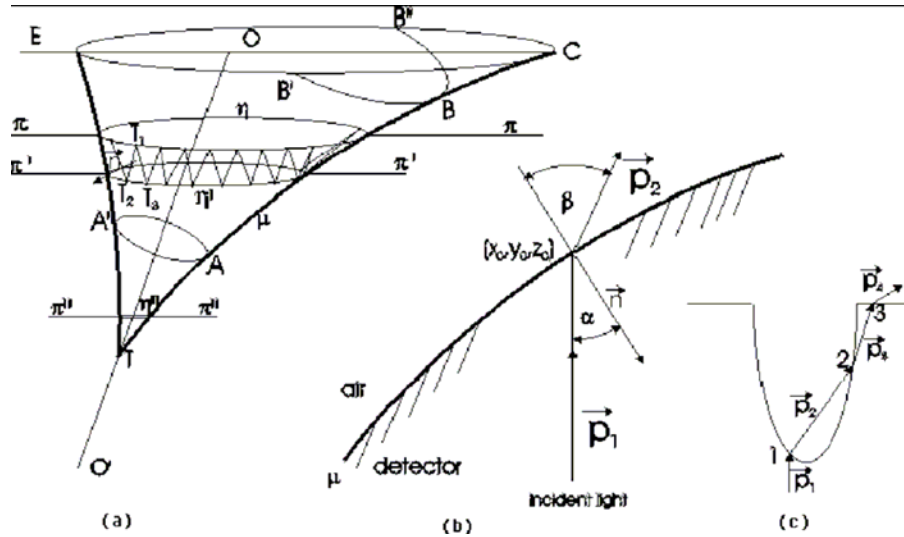
Figure 4. (a) Creation of the 3D mesh that represents the track. (b) Ray refraction on the surface between detector and air. (c) One ray path through the track.

Plotting the track profile in PADC and cellulose nitrate SSNTDs were described by Nikezic and Yu (2003b). Furthermore, the computer program TRACK_TEST which performs this plotting and creates the 3D mesh, was described and published by Nikezic and Yu (2006), and can be downloaded from our webpage http://www.cityu.edu.hk/ap/nru/test.htm. One example of output results of the TRACK_TEST program is the 3D graph shown in Figure 5.
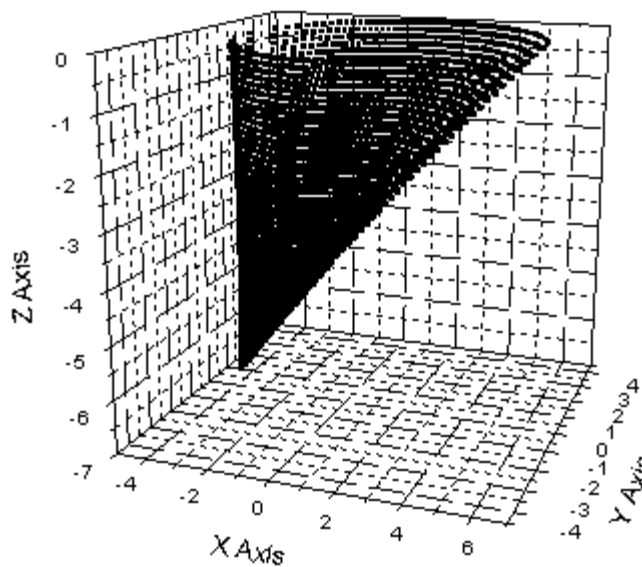


Figure 5. A 3D mesh representing the track generated by an alpha particle in a PADC SSNTD. $E_\alpha = 5$ MeV, incident angle $\theta = 60^o$ and removed layer = 7.2 μm.

The mesh presented in Figure 5 represents the track in a PADC SSNTD generated by an alpha particle with energy of 5 MeV under an incident angle of $60^\circ$ and for a removed layer of 7.2 μm during etching. A total of 4900 points exist in this mesh, which were generated as a result of rotation of 49 points around the track axis, with 100 points recorded on each circle. This track has a depth of 6.7 μm and a major axis of 9.3 μm. To estimate the minor axis, another more convenient view should be chosen.

For each studied track, such a mesh must be created. This will not be problematic if only one track is considered. However, if many tracks have to be studied simultaneously, there might be problems with the computer memory.


## 4.2. Application of Ray Tracing to Light Through the Track

The next step is the determination of normal lines to all triangles as described above. Here, the transmission mode of the optical microscope is considered, so the light comes from the bottom as shown in Figure 4(b). The light ray is represented by the vertical line which intersects the track wall (represented by the curve $\mu$) at the point $(x_0, y_0, z_0)$, the coordinates of which are the geometrical means of those for the apices of the concerned triangle. The vector $\vec{p}_1$ determines the direction of the incident ray. Here, we assume that all the incident light rays are perpendicular to the general surface of the detector (i.e., regions without tracks). It is not appropriate to assume that the rays come from a cone for such a small object as the track. In addition, the microscope used in experimental work has a lens between the lamp and the object, which creates a parallel beam of light. The vector $\vec{p}_2$ represents the light ray after refraction at point $(x_0, y_0, z_0)$ in the track wall. The vector $\vec{p}_2$ is determined through the set of equations describing light refraction given in Eq. (9).

In some cases, the light ray may return back to the detector. This more complex case is schematically shown in Figure 4(c). The new entrance point (denoted by 2) on the track wall has to be determined. Another refraction occurs at that point and a further reduction in the ray intensity has to be determined. A total of three refractions are possible for a light ray (see Figure 2(c)). In this case, the ray paths through the points 1, 2 and 3 are defined by four vectors, namely, $\vec{p}_1, \vec{p}_2, \vec{p}_3$ and $\vec{p}_4$, each of them being determined using formulas similar to those given above. At points 1 and 3, where the ray comes to the detector-air interface, total internal reflection is also possible if the incident angle is larger than critical angle. In this case, the direction of the reflected ray is calculated according to the set of equations given in Eq. (7).

The reduction in the light intensity due to refraction on the detector-air surface is calculated by the formula given by Skvarč (1999) (as their Eq. (2)). Since the refractive index of commonly used detectors are relatively small, the reduction of intensity is less than a few percents. In the case of several refractions, and large incident angles, the total reduction in the light intensity can reach 40%. This is responsible for creation of different gray levels in some parts of the track images. Those elements which totally reflect the light rays are completely dark.

## 4.3. Gray Level of the Tracks

The procedures described above are repeated for each element of the track and the relative light intensity for each element is calculated. The light intensities coming from separate elements are segregated into intensity "numbers" by dividing the range from no transmission through the detector (completely dark) to total transmission (completely bright) linearly into 256 intervals, with the intensity number 0 representing completely dark while 255 representing completely bright. The intensity number represents the gray level of an element obtained from ray tracing.

Figure 6 gives six sample results, where the tracks are in PADC SSTNDs generated by alpha particles with an energy of 5 MeV under normal incidence, with etching time of 5, 10, 15, 20 and 25 h. The bulk etch rate is assumed to be 1.2 μm/h. The track appearance has been simulated using the ray tracing method. Each has been represented with 99×200 points. Dark areas are obtained from elements that totally reflect the light rays. The track obtained for the shortest etching time of 5 h, is completely dark, indicating that all its elements have totally reflected the light. This is due to the steep wall of the track so that incidence angle is larger than the critical angle for total reflection. With the etching time increased to 10 h, the track is slightly overetched, and a rounded part is created around the end of the particle trajectory. The track wall of this part is not steep and light can pass through the detector-air interface without total reflection, and this part is thus seen as a bright spot. With the etching time further increased to 15 and 20 h, the rounded portion of the track is increased, and the bright spot becomes larger and occupies a larger part of the track. After chemical etching for 25 h, the track is fully spherical and the majority of track is bright, but the dark circumference is still distinct so this track can easily be distinguished from the rest of the detector surface in the readout phase.
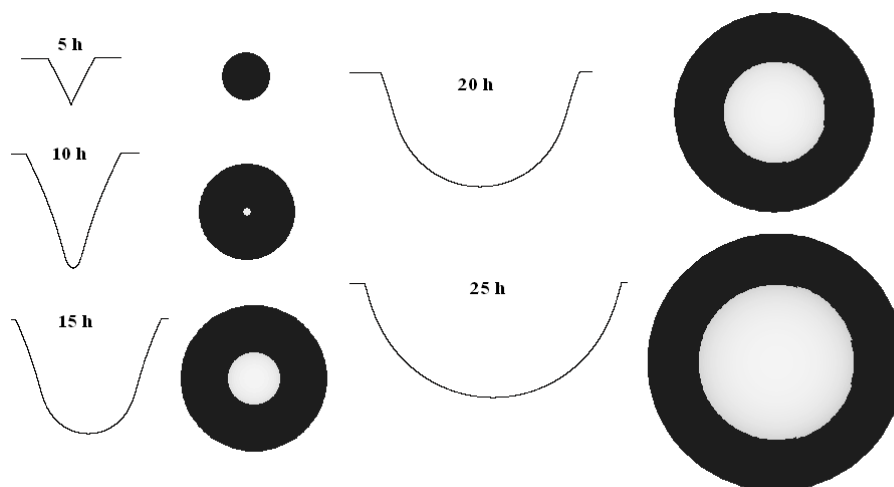


Figure 6. Track profiles and corresponding images as seen from above, for tracks at different developmental stages, i.e., after etching for 5, 10, 15, 20 and 25 h. The tracks are in PADC SSTNDs generated by alpha particles with an energy of 5 MeV under normal incidence. The bulk etch rate is 1.2 μm/h.
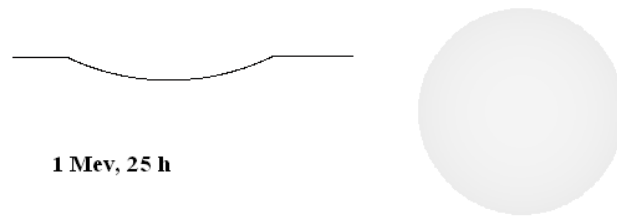
**1 Mev, 25 h**

Figure 7. Track profile and the corresponding image as seen from above, for a track etched for 25 h. The track is in a PADC SSTND generated by an alpha particle with an energy of 1 MeV under normal incidence. The bulk etch rate is 1.2 μm/h.
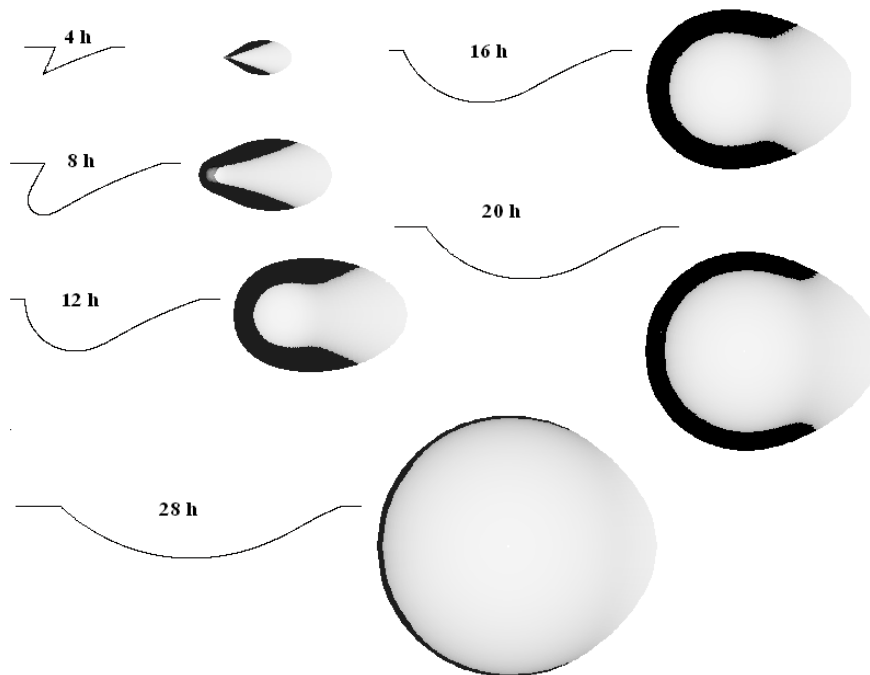


Figure 8. Track profiles and corresponding images as seen from above, for tracks at different developmental stages, i.e., after etching for 4, 8, 12, 16, 20 and 28 h. The tracks are in PADC SSTNDs generated by alpha particles with an energy of 4 MeV with an incident angle of 45°. The bulk etch rate is 1.2 μm/h.

In contrary to the previous cases, the track in a PADC SSNTD generated by a 1 MeV alpha particle will lose its dark circumference after 25 h of etching, and appears as a slightly bright circular spot. This track may be easily overlooked during the readout step because it does not stand out distinctly from the background.

In Figure 8, tracks in PADC SSNTDs generated by 4 MeV alpha particles with oblique incidence and for different etching time are presented. The images are more complex than those generated by alpha particles with normal incidence, because the right portions of the images are not dark and the corresponding track boundaries cannot be seen clearly. As such, the major axes of the track openings might be determined with larger uncertainties. Very bright spots are seen within the track openings when almost flat bottoms are developed. With

prolonged etching, the bright spot increases in size and occupies a larger portion of the track area. At the same time, the dark circumference due to total reflection becomes smaller and smaller, and almost disappears after 28 h of etching when the track is in the spherical form.

## 4.4. Scattering from One Track

Besides calculations of gray levels for a track, it is also possible to determine the distribution of light scattered by the track. The methodology is similar to that described above, with additional steps to determine the direction of the scattered light. To calculate the intensity of the light ray scattered from the etched alpha-particle track, a "detection hemisphere" with a radius $R$, which is much larger than the track dimensions, is constructed with the center at the point where the particle trajectory intersects with the post-etched detector surface. The hemisphere is then divided into surface elements with steps of $\Delta\varphi = 1^{\circ}$ and $\Delta\theta = 1^{\circ}$, so a total of 32400 elements are used. The surface areas of the elements are given by $\Delta S = R^2 \sin\theta \, \Delta\theta \, \Delta\varphi$, and each surface element is characterized by two angles, or with two index variables in the computer program. Although the calculations are performed for the whole hemisphere, the distributions are given only in terms of the two angles, $\theta$ and $\varphi$. The coordinate system is chosen in the following way. The origin is at the point where the particle trajectory intersects with the post-etched detector surface. The $z$-axis is perpendicular to the detector surface and is directed out of the detector body. The $x$-axis is along the detector surface and represents the projection of the particle trajectory onto the detector surface. The $y$-axis is also along the detector surface and is orthogonal to the $x$- and $z$-axes. In such a geometry, the tracks are always symmetrical with respect to the plane $y = 0$. Therefore, the distribution of scattered light should also be symmetrical.

Details of this problem was discussed by Nikezic and Yu (2008a), and the related computer program called TRACK_VISION was described by Nikezic and Yu (2008b). The program is also downloadable from the web site http://www.cityu.edu.hk/ap/nru/vision.htm.

One example of calculation of scattered light distribution is given in Figure 9. Here, an etched track in a PADC SSNTD is generated by an alpha particle with an incident energy of 5 MeV and an incident angle of $60^{\circ}$, and for 6 h etching with a bulk etch rate of 1.2 μm/h. The profile of this track as well as the simulated optical appearance of this track as viewed from above are both determined using TRACK_VISION 1.0, which are shown in Figure 9. The angular distributions of the scattered light are also shown in Figure 9.

Here, the track depth is 7.4 μm, while the major and minor axes are 10.1 and 8.26 μm, respectively. This track is in the semi-conical phase. A part of the track wall (the left portion of the track shown in the upper panel of Figure 9) is almost vertical and this is in fact extended to the right portion in the 3D space. These steep walls have led to total internal reflection of light, which is revealed as the dark part of the track when viewed from the above. The other part of the track wall (the right portion of the track shown in the upper panel of Figure 9) has such an inclination angle so that light can pass with some refraction and this portion is revealed as the bright part of the track when viewed from the above.

In the lower panel of Figure 9, the distribution of scattered light with the angle $\theta$ is shown. Here, a very strong peak exists at about $30^{\circ}$. This may be explained through the analysis of inclination of the right part of the tracks, and also the incident and refracted angles

of the light rays. Explanation of the distribution of the angle $\varphi$ is more complicated, but we can note that this distribution is symmetrical as expected. If the track is generated from an alpha particle with normal incidence, the distribution along the angle $\varphi$ will be uniform.

## 4.5. Scattering from an Assembly of Tracks

It will be difficult to design an experiment to study light scattering from a single track, of which the results have been described in section 5 above. In contrary, an assembly of tracks always exists in exposed and etched SSNTDs. In addition, the light intensity scattered from one track may be too small to be measured. An assemble of tracks can be generated in a SSNTD through irradiation with radon and its short-lived progeny, or irradiation with some ions under well-defined conditions in experiments with ion sources. The geometrical treatment of light scattering on one track described above can also be applied here, but with some modifications in the scoring procedures and in the interpretation of the final results. Here, the case of irradiation with radon and its short-lived progeny will be elaborated in more details.

When a single track was considered, the $z$-axis was normal to the detector surface, the $x$-axis was on the post-etching surface of the detector and was along the major axis of the track, and the $y$-axis was normal to the $x$-axis and was also on the post-etching surface of the detector. However, in the case of irradiation with radon and its short-lived progeny, there will be tracks with different orientations with respect to the angle $\varphi$ as shown in Figure 10, where two tracks $T_1$ and $T_2$ are presented. The major axis of the track $T_1$ overlaps with the $x$-axis of the coordinate system, and the track center coincides with the origin of the coordinate system. In the previous section, the light scattering was calculated only from tracks located as $T_1$.

Track $T_2$ is located at another position in the detector, and it is analyzed in the following ways: (1) the origin of the coordinate system is translated to the center of $T_2$ and the system is then rotated for the angle $\varphi$; (2) the scattering of light is then calculated from $T_2$ in the new translated and rotated coordinate system; (3) the last step is to return back to the basic coordinate system $xOy$. The calculated scattering pattern from a single track has to be rotated back for the angle $-\varphi$.

In our model, a circular PADC film with an area of 1 cm$^2$ is considered, and the origin of the coordinate system is chosen to be at the center of the detector. Circular detector geometry is adopted for the sake of simplicity. To calculate the intensity of the scattered light, a hemisphere with radius of 10 cm (ensuring that it is much larger than the radius of a detector) is constructed with the center located at the origin

A scattered light ray that exits from the detector material should intersect with the hemisphere at a point that can be determined by $\varphi_{sc}$ and $\theta_{sc}$, and these angles determined the approximate scattering direction. The situation is also illustrated in Figure 10, where one light beam is scattered by $T_2$.
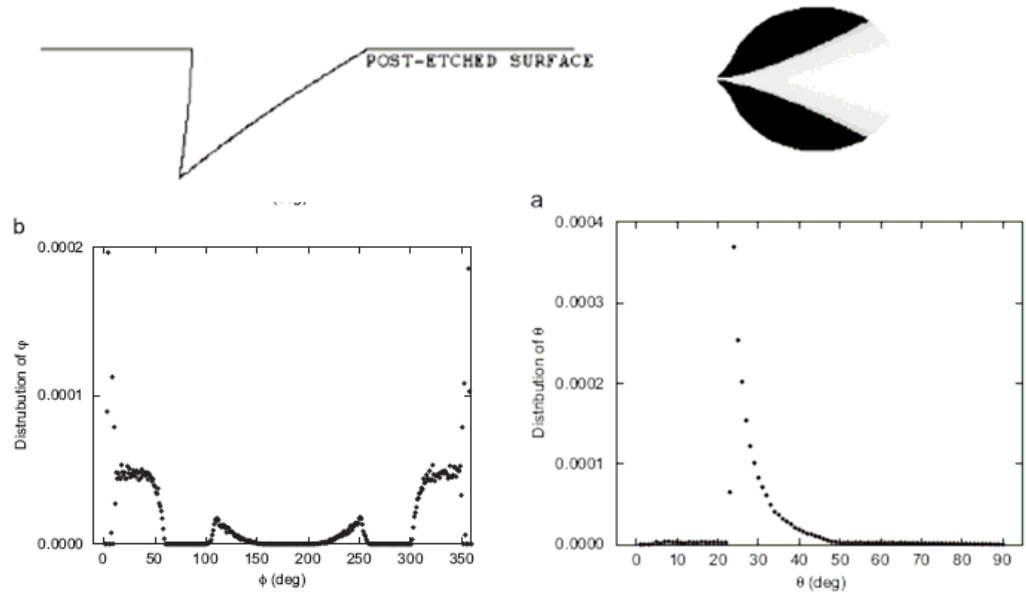
Figure 9. *Upper panel:* an etched track in a PADC SSNTD generated by an alpha particle with an incident energy of 5 MeV and an incident angle of 60°, and for 6 h etching with a bulk etch rate of 1.2 μm/h. The track profile is shown on the left, while the simulated optical appearance of the track as viewed from above is shown on the right. *Lower panel:* angular distributions of the scattered light, for angle $\varphi$ (left) and angle $\theta$ (right) for the track shown in the upper panel.
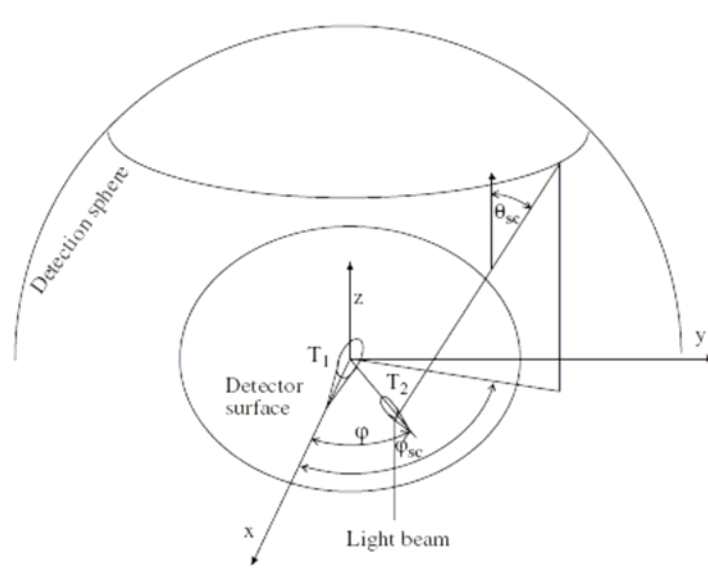


Figure 10. Coordinate system employed for the present study. The major axis of the track $T_1$ lies along the *x*-axis. The tip of $T_1$ is in the *xOz* plane. The major axis of the track $T_2$ is determined with the angle $\varphi$. The detection hemisphere is also shown.

This model is applied to the case of detector irradiation by alpha particles from radon and its short-lived progeny. The tracks in the PADC film originate from alpha particles emitted by radon ($^{222}$Rn) and its short-lived progeny $^{214}$Po and $^{218}$Po, with energies 5.49, 6 and 7.69

MeV, respectively. A mixture of radon and its progeny in air is usually characterized by the so-called "equilibrium factor". The simulation starts with sampling of an emitter which can be $^{222}$Rn, $^{214}$Po or $^{218}$Po. If the concentrations of these alpha-particle emitters are denoted as $C_0$, $C_1$ and $C_4$, respectively, the total alpha-particle activity $C_{tot}$ is given by $C_{tot} = (C_0+C_1+C_4)$. Three ratios are defined as $A = C_0/C_{tot}$, $B = C_1/C_{tot}$ and $C = C_4/C_{tot}$. The standard method of discrete event sampling is applied to "choose" an alpha particle as follows. The random number generator is invoked to get one random number $\gamma$, if $\gamma < A$, the emitter is chosen as $^{222}$Rn; if $A < \gamma < (A+B)$, the emitter is $^{218}$Po; and if $(A+B) < \gamma < 1$, the emitter is $^{214}$Po. After choosing the emitter (and thus the corresponding alpha-particle energy), the emission point and direction are also sampled. The next step in the simulation is to check whether the alpha particle hits the detector considering its flight direction and range in air. If not, this alpha particle will be discarded and the simulation loop is restarted, choosing a new alpha particle. Obviously, the cases where the alpha particles hit the detector and leave latent tracks in it are more important. If a visible track is formed from that latent track due to subsequent chemical etching, the three-dimensional coordinates of the track are calculated. The last step will involve the simulation of light propagation through the track and calculations of the angular distribution (in $\theta$ and $\varphi$) of the scattered light. To perform the last step of simulation, a computer program TRACK_VISION.F90 mentioned above and described previously by Nikezic and Yu (2008b) is used as a subroutine. Information about the scattering direction is stored in the computer memory. After this, the construction of one track and calculation of light scattered by it are completed. A new alpha particle will then be chosen and all the procedures are repeated again. The intensity of light scattered from a track in a particular direction is added to the total intensity in that direction summed from previous calculations, so that the result for a given assembly of tracks can be obtained. The simulation is terminated when the predetermined number of tracks is achieved.

One specific problem is noted here. The tracks generated by alpha particles from radon and its short-lived progeny, as mentioned above, can be very different in size and shape with various scattering characteristics. Here, a track is represented as a mesh of planar elements with a size of approximately of $1 \times 1$ $\mu m^2$. Each element will scatter light in a defined direction. The intensity of light scattered by an element has then to be multiplied with a weighting factor $\omega_i$, which is equal to the ratio between the surface area of the $i^{th}$ element (projected onto the detector surface) and the total surface area of the detector.

### Example 1. Dependence of scattered intensity on track density

The scattered light intensity is dependent on the track density. This is expected since more tracks will scatter more light. To study this dependence, the number of tracks on a 1 cm$^2$ detector surface is varied between 100 and 2000 for the three different etching durations of 4, 8 and 12 h. The results are given in Figure 11. The ordinate gives the ratio $I/I_0$, where the total scattered light intensity $I$ is evaluated by integrating over all angles $\varphi$ (between 0 and $2\pi$) and $\theta$ (between 0 and $\pi$). A linear dependence is apparent, which is very promising in enabling a practical application. The increase in the scattered intensity with the etching time is also expected because larger tracks scatter more light.
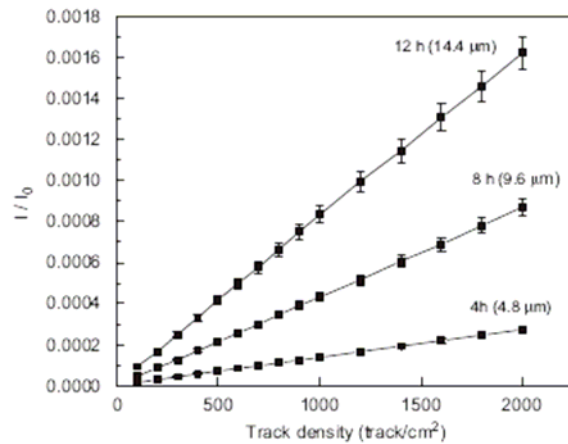
Figure 11. Relative intensity of the scattered light as a function of the track density with the etching time in $h$ (or removed layer in μm) as a parameter (Nikezic and Yu 2009).

### *Example 2. Angular distribution of the scattered light*

Figure 12 shows the distribution of scattered light intensity with respect to the angle $\theta$ for different ratios of $F_1$ and $F_4$, where $F_1 = C_{218_{Po}} / C_{222_{Rn}}$, $F_4 = C_{214_{Po}} / C_{222_{Rn}}$ and $C_{222_{Rn}}$, $C_{218_{Po}}$ and $C_{214_{Po}}$ are the airborne activity concentrations of $^{222}$Rn, $^{218}$Po and $^{214}$Po. In the simulations, the whole interval of angle $\theta$ between $0^o$ and $90^o$ was divided into 90 intervals, with increments of $1^o$. Calculations have been performed for 1000 tracks/cm$^2$ on a PADC film for 14 h of etching (corresponding to 16.8 μm of removed layer during chemical etching). Insets show the semi-logarithmic presentations.
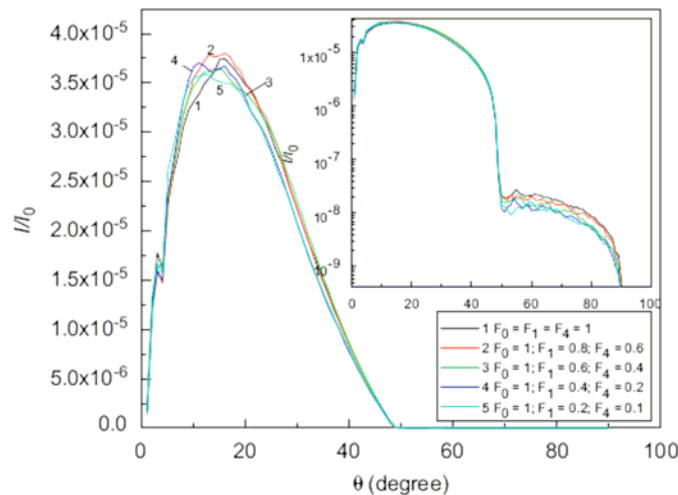


Figure 12. Distribution of scattered light intensity with respect to the angle $\theta$ for different ratios of $F_1$ and $F_4$. In the simulations, the whole interval of angle $\theta$ between $0^o$ and $90^o$ was divided into 90 intervals, with increments of $1^o$. Calculations have been performed for 1000 tracks/cm$^2$ on a PADC film for 14 h of etching. Insets show the semi-logarithmic presentations. (Adopted from Nikezic and Yu 2009.)

From Figure 12, we can see that the distributions have maximums between $10^o$ and $20^o$ and fall to very small values beyond $50^o$. In addition to scattering at small angles, the light can be scattered at very large angles, up to $80^o$, but with very small intensities. These results are better seen in the semi-logarithmic presentations shown as insets in Figure 12. The dependence on the radon progeny ratios is very weak (viz., all curves are close to one another).

Here, for large scattering angles, the distinction among the curves corresponding to different equilibrium factors is very weak, and it is dubious whether this small separation can be used for determination of the equilibrium factor, considering the very low intensity of light scattered at large angles.

## 5. CONCLUSIONS

In this chapter, application of the ray tracing method on etched ion tracks in a solid state nuclear track detector (PADC film) has been described. The method is shown to be useful to simulate the appearance of tracks generated with various irradiation and etching conditions. The method also enables calculation of gray levels for particular tracks elements and provides the distribution of gray levels along the track. Some track parameters, such as the major and minor axes and projected lengths are easily measurable under a common optical microscope. However, measurements of the track depth as well as the track profile are not straightforward. Several methods were explored in the past for track depth measurements, and many of these either have limitations or involve tedious procedures (e.g., Yamamoto et al., 1997, Meesen and VanOostveldt, 1997, Yu et al., 2004, Ng et al., 2007). Furthermore, the energy of the incident particle is better related to the track depth (the track depth is actually equal to the particle range in the over-etched phase) than to the parameters of the track opening (i.e., major and minor axes). It will be of great interest to develop the reversed model and the corresponding computer programs, which together will enable the determination of the track depth and the track profile, based on the track shape, track parameters and the gray levels of track elements.

## ACKNOWLEDGMENT

## REFERENCES

Assunção, MPM; Pugliesi, R; De Menezes, MO. *Appl Radiat Isotopes*., 1994, 45, 851-855.
Cartwright, BG; Shirk, EK; Price. PB. *Nucl Instrum Meth*., 1978, 153, 457-460.
Ditlov, V. *Radiat Meas*., 1995, 25, 89-94.
Fews, AP. *Nucl Instrum Meth B*., 1992, 72, 91-103.
Fews, AP; Henshaw, DL. *Nucl Instrum Meth*., 1982, 197, 517-529.

Fleischer, RL. *Tracks to innovation : nuclear tracks in science and technology*., New York : Springer, 1998.

Fleischer, RL; Price, PB; Walker, RM. *Annu Rev Nucl S.*, 1965, 15, 1-28.

Fleischer, RL; Price, PB; Walker, RM. *Nuclear Tracks in Solids*, University of California Press, Berkley, 1975.

Fromm, M; Chambaudet, A; Membrey, F. *Nucl Tracks Radiat Meas.*, 1988, 15, 115-118.

Groetz, JE; Lacourt, A; Chambaudet, A. *Nucl Instrum Meth B.*, 1998, 142, 503-514.

Groetz, JE; Lacourt, A; Meyer, P; Fromm, M; Chambaudet, A; Potter, J. *Radiat Prot Dosim.*, 1999, 85, 447-450.

Harvey, JR; Weeks, AR. *Radiat Prot Dosim.*, 1987, 20, 89-93.

Henke, PR; Benton, E. *Nucl Instrum Meth.*, 1971, 97, 483-489.

McNulty, PJ; Palmer, SR; Cooke, DD. *In: Proceedings of the 11$^{th}$ International Conference on SSNTD*, Editors, Fowler PH; VM. Clapham. Pergamon Press, Oxford, UK, 1982, 807-813.

Meesen, G; Van Oostveldt, P. *Radiat Meas.*, 1997, 28, 845-848.

Meyer, P; Groetz, J.E; Fromm, M; Lacourt, A; Chambaudet, A. *Radiat Meas.*, 1997, 28, 423-428.

Ng, F.M.F; Luk, K.Y; Nikezic, D; K.N. Yu. Nucl Instrum Meth B. 2007, 263, 266-270

Nikezic, D; Kostic, D; Yip, CWY; Yu., KN. *Radiat Meas.*, 2006, 41, 253-256.

Nikezic, D; Ng, FMF; Yip, CWY; KN. Yu. *Radiat Meas.*, 2005, 40, 375-379.

Nikezic, D; Yu, KN. *Radiat Meas.*, 2003a, 37, 39-45.

Nikezic, D; Yu, KN. *Radiat Meas.*, 2003b, 37, 595-601.

Nikezic D; Yu, KN. *Mat Sci Eng R.*, 2004, 46, 51-123

Nikezic, D; Yu, KN. *Comput Phys Commun.*, 2006, 174, 160-165.

Nikezic, D; Yu, KN. *Radiat Meas.*, 2008a, 43, 1417-1422.

Nikezic, D; Yu, KN. *Comput Phys Commun.*, 2008b, 178, 591-595.

Nikezic, D; Yu, KN. *Nucl Instrum Meth A.*, 2009, 602, 545-551.

Popov, PC; Pressyanov, DS. *Radiat Meas.*, 1997, 27, 27-30.

Silk, ECH; Barnes, RS. *Philos Mag.*, 1959, 4, 970-972.

Skvarč, J. *Radiat Meas.*, 1999, 31, 217-222.

Skvarč, J; Ilic, R; Kodre, A. *Nucl Instrum Meth B.*, 1992, 71, 60-64.

Somogyi, G. *Nucl Instrum Meth.*, 1980, 173, 21-42.

Somogyi, G; Szalay, AS. *Nucl Instrum Meth.*, 1973, 109, 211-232.

Yamamoto, M; Yasuda, N; Kaizuka, Y; Yamagishi, M; Kanai, T; Ishigure, N; Furukawa, A; Kurano, M; Miyahara, N; Nakazawa, M; Doke, T; Ogura, K. *Radiat Meas.*, 1997, 28, 227-230.

Young, DA. *Nature.*, 1958, 182, 375-377.

Yu, KN; Lee, HHW; Wong, AWT; Law, YL; Cheung, SFL; Nikezic, D; Ng. FMF. *Nucl Instrum Meth B.*, 2007, 263, 271-278.

Yu, KN; Ng, FMF; Ho, JPY; Yip, CW; Nikezic, D. *Radiat Prot Dosim.*, 2004, 111, 93-96

Yu, KN; Nikezic, D; Ng, FMF; Leung, JKC. *Radiat Meas.*, 2005, 40, 560-568.